Acousto-dielectric Tweezers for Size-insensitive Manipulation and Biophysical Characterization of Single Cells

Liang Shen ^{a,b}, Zhenhua Tian ^{c,*}, Jinxin Zhang ^a, Haodong Zhu ^a, Kaichun Yang ^a, Teng Li ^c, Joseph Rich ^d, Neil Upreti ^d, Nanjing Hao ^a, Zhichao Pei ^a, Geonsoo Jin ^a, Shujie Yang ^a, Yaosi Liang ^c, Wang Chaohui ^{b,*}, Tony Jun Huang ^{a,*}

Highlights

Establish an acousto-dielectric tweezing mechanism.

High-throughput single cell measurement of acousto-dielectric factor.

Separate different kinds of cells with the same diameter distribution.

Concurrent acoustic and electrical properties measurement of single cells.

Abstract

The intrinsic biophysical properties of cells, such as mechanical, acoustic, and electrical properties, are valuable indicators of a cell's function and state. However, traditional single-cell biophysical characterization methods are hindered by limited measurable properties, time-consuming procedures, and complex system setups. This study presents acousto-dielectric tweezers that leverage the balance between controllable acoustophoretic and dielectrophoretic forces applied on cells through surface acoustic waves and alternating current electric fields, respectively. Particularly, the balanced acoustophoretic and dielectrophoretic forces can trap cells at equilibrium positions independent of the cell size to differentiate between various cell-intrinsic mechanical, acoustic, and electrical properties. Experimental results show our mechanism has the potential for applications in single-cell analysis, size-insensitive cell separation, and cell phenotyping, which are all primarily based on cells' intrinsic biophysical properties. Our results also show the measured equilibrium position of a cell can inversely determine multiple biophysical properties, including membrane capacitance, cytoplasm conductivity,

^a Department of Mechanical Engineering and Materials Science, Duke University, Durham, NC, 27708, USA

^b State Key Laboratory of Manufacturing Systems Engineering, Xi'an Jiaotong University, Xi'an, Shaanxi, 710049, China

^c Department of Mechanical Engineering, Virginia Polytechnic Institute and State University, Blacksburg, VA, 24061, USA

^d Department of Biomedical Engineering, Duke University, Durham, NC, 27708, USA

^e Department of Pharmacology and Cancer Biology, Duke University, Durham, NC, 27708, USA

^{*} Corresponding author: Z. T. (tianz@vt.edu), W.C. (chhw@mail.xjtu.edu.cn), T.H. (tony.huang@duke.edu)

and acoustic contrast factor. With these features, our acousto-dielectric tweezing mechanism is a valuable addition to the resources available for biophysical property-based biological and medical research.

Keywords: acoustofluidics, acousto-dielectric tweezers, size-insensitive manipulation, cell biophysical characterization

1. Introduction

Label-free, quantitative characterization of cell-intrinsic biophysical properties, such as acoustic (Augustsson et al. 2016; Guo et al. 2021; Hwang et al. 2016; Mishra et al. 2014), mechanical (Fregin et al. 2019; Gossett et al. 2012; Otto et al. 2015; Panhwar et al. 2020; Rosendahl et al. 2018; Urbanska et al. 2020), optical (Mugnano et al. 2018), and electrical properties (Yang et al. 2019; Zhao et al. 2013; Zhao et al. 2016), has garnered increasing attention in recent years. Due to their sensitivity to changes in the membrane, cytoplasm, cytoskeleton, and nucleus of cells, biophysical properties are valuable indicators of cell states and functions. The biophysical properties of cells have also shown great potential for cell phenotyping and single-cell analyses, such as characterizing stem cell differentiation, immune cell activation, and metabolic states (Koch et al. 2017; Kooiman et al. 2014; Lautenschläger et al. 2009; Loo et al. 2019; Maloney et al. 2010; Munder et al. 2016; Pagliara et al. 2014).

When characterizing the biophysical properties of single cells, early methods such as atomic force microscopy (Alcaraz et al. 2003; Kuznetsova et al. 2007), micropipette aspiration (Guo et al. 2012; Hochmuth 2000), optical stretching (Mills et al. 2004), patch clamping (Lange et al. 2015; Nyberg et al. 2017), and nanoprobes (Actis et al. 2014) suffered from low throughputs, time-consuming procedures, and complex, specialized systems. Alternatively, microfluidic devices that utilize hydrodynamic (Rosendahl et al. 2018), acoustophoretic (Baudoin et al. 2020; Destgeer and Sung 2015; Lin et al. 2012; Yeo and Friend 2014), and dielectrophoretic (Pethig 2010) (DEP) forces have been developed to achieve high-throughput characterization of single-cell biophysical properties, such as cell deformability (Rosendahl et al. 2018), acoustic contrast factors (Wang et al. 2019), and cell electrical properties (Zhang et al. 2020). Given the advances of previous studies, none of them are capable of simultaneously characterizing the acoustic and electrical properties of cells. This limitation prevents the concurrent use of multiple biophysical properties for multi-parameter cell phenotyping and single-cell analysis. In addition, current potential field-based cell manipulation methods, such as acoustic (Bruus 2012; Liang

et al. 2018; Zhang 2018), optic (Harada and Asakura 1996), magnetic (Ahmed et al. 2017; Durmus et al. 2015; Lipfert et al. 2009), and dielectric tweezers (Kim et al. 2019; Wang et al. 2007), are sensitive to cell sizes. This limitation inhibits the manipulation and separation of cell populations with similarly sized cells.

To address the limitations listed above, this study presents an acousto-dielectric tweezing mechanism based on the application of balanced acoustic radiation and DEP forces on cells. The tweezing mechanism makes use of controlled surface acoustic waves (SAWs) and alternating current (AC) electric fields to apply acoustic radiation and DEP forces (Bernassau et al. 2013; Laurell et al. 2007; Ma et al. 2020) in opposite directions on cells within a microchannel. As a result, cells in the SAW and AC electric fields can be translated to equilibrium positions (namely, equi-acousto-dielectric positions) where they experience balanced acoustic radiation and DEP forces. Notably, our theoretical and experimental studies show that the equi-acousto-dielectric position is insensitive to the cell volume, while still remaining sensitive to the acousto-dielectric factor (i.e., a dimensionless parameter dependent on the intrinsic acoustic and electrical properties of the cell). Our studies also show cells with different acousto-dielectric factors can be translated to distinct equi-acousto-dielectric positions. Based on these features, we demonstrated our acousto-dielectric tweezers have the potential for biophysical propertybased, size-insensitive separation of cells, single-cell biophysical analysis, and cell phenotyping. The acousto-dielectric mechanism also shows promise for characterizing multiple biophysical properties such as membrane capacitance, cytoplasm conductivity, and acoustic contrast factor. We expect the presented acousto-dielectric tweezing mechanism will lead to valuable biophysical analysis platforms for biological and medical research (Hao et al. 2022; Rufo et al. 2022a; Rufo et al. 2022b).

2. Materials and Methods

2.1. Cell sample preparation

Prior to the experiments, HeLa, 293T, and MCF7 cells (ATCC) were cultured in Dulbecco's Modified

Eagle's media (Gibco, Life Technologies), which contained 10% fetal bovine serum (Gibco, Life Technologies) and 1% penicillin-streptomycin (Mediatech). Jurkat cells (ATCC) were cultured in RPMI-1640 media (Gibco, Life Technologies) supplemented with 10% fetal bovine serum and 1% penicillin-streptomycin. All the cells were cultured in an incubator (Heracell Vios 160i CO₂ incubator, Thermo Scientific) at a temperature of 37°C and a CO₂ level of 5% (Yang et al. 2022). To observe live cells, the cultured cells were stained with calcein-AM (C3100MP, Life Technologies), washed with phosphate-buffered saline (Gibco, Life Technologies) three times, and resuspended in a tweezing buffer at a concentration of ~1×10⁶ ml⁻¹. Tweezing buffer A was prepared by mixing 8.5% (w/w) sucrose (S9378, Sigma), 0.3% (w/w) glucose (G82370, Sigma), deionized water, and phosphate-buffered saline. Tweezing buffer B was prepared by mixing 8.5% (w/w) sucrose (S9378, Sigma), 0.3% (w/w) glucose (G82370, Sigma), deionized water, and phosphate-buffered saline (Shafiee et al. 2009). The material properties (including densities, compressibility values, viscosities, relative permittivity values, and conductivities) of the two buffers are listed in Supplementary Table 1.

2.2. Fabrication and operation of acousto-dielectric chips

A photo of a fabricated acousto-dielectric chip is provided in Fig. S1. The chip has a lithium niobate (LiNbO₃) substrate (Y128-cut, Precision Micro-Optics) with a pair of interdigital transducers (IDTs) for generating standing SAWs and tri-port electrodes for generating an AC electric field. A polydimethylsiloxane-based microchannel with an inner width of 500 µm is bonded to the LiNbO₃ substrate. The microchannel, IDTs, and tri-port electrodes are arranged symmetrically with respect to the chip's centerline. This is meant to ensure generated SAWs have an antinode line which coincides with both the microchannel and the tri-port electrodes' centerlines. The polydimethylsiloxane-based microchannel was fabricated by following typical soft lithography and mold replica procedures (Chung et al. 2007). The IDTs and electrodes on the LiNbO₃ substrate were fabricated with 50 nm Au/5 nm Cr layers by following typical electrode fabrication procedures such as photolithography, e-beam

evaporation, and lift off (Chen et al. 2021; Mei et al. 2020). Each IDT has 25 pairs of interdigital electrodes with a finger width of 125 μm, a finger spacing of 125 μm, and an aperture size of 8 mm. The IDT's frequency response was characterized by using a network analyzer (E5063A, Keysight). The S11 frequency response curve (Fig. S4) acquired from this analysis shows that the resonant frequency is around 7.86 MHz (Tao et al. 2018).

While performing experiments, our fabricated acousto-dielectric chip was mounted on the sample stage of a fluorescence microscope (TE2000-U, Nikon). Cells suspended in a tweezing buffer were loaded into a 1-mL syringe (309659, Becton Dickinson) and pumped into the microchannel through an inlet. A tweezing buffer without cells was loaded into another 1-mL syringe and pumped into the microchannel to create the sheath flows necessary for keeping cells near the centerline of the microchannel. The flow rates of the buffers were controlled by a high-precision automated pumping system (neMESYS, CETONI). To generate the standing SAWs used to apply acoustic radiation forces on cells, the IDT's input signal was produced by a function generator (AFG3102C, Tektronix) at a frequency of f_a (the same as the pre-characterized resonant frequency of IDTs) and then amplified by a power amplifier (25A250A, Amplifier Research). To generate the AC electric field used to apply DEP forces on cells, another function generator (AFG3102C, Tektronix) was connected to the tri-port electrodes and a signal with two frequencies was produced, i.e., f_a for canceling the piezoelectric voltages induced by the standing SAWs and f_e for enabling the DEP effect (Chen et al. 2013). The related circuit connection diagrams for sending input signals to IDTs and tri-port electrodes are given in Fig. S5. As cells flowed through the microchannel during the experiments, a CCD camera (CoolSNAP HQ2, Photometrics) installed on the microscope was used to monitor the area of interest near the channel outlet (Tian et al. 2019).

2.3. Calibration of an acousto-dielectric field function

To obtain a calibrated acousto-dielectric field function $\Psi_c(x)$, we performed experiments with fluorescent polystyrene microparticles (Bangs Laboratories Inc.) with the known material properties listed in Supplementary Table 1. The polystyrene microparticles were suspended in our previously prepared Tweezing buffer A. Calibration experiments were performed at two conditions, one with exclusively SAWs and the other with only an AC electric field present. In the first scenario, SAWs were generated by IDTs with a 30 Vpp input signal at 7.86 MHz, and the SAW-induced motions of the microparticles were recorded with a microscope camera. In the second scenario, an AC electric field was generated by tri-port electrodes with a 7 Vpp signal at 30 kHz and the DEP-induced motions of microparticles were recorded.

We analyzed the time-dependent trajectories of multiple microparticles and calculated the particle velocities at different x-positions within the microchannel. Fig. S2a and S2b provide statistical results of the measured SAW-induced velocities v_{ps-a} and DEP-induced velocities v_{ps-e} . These characterized velocities, as well as the material properties of the tweezing buffer and polystyrene particles used, were substituted into a calculation method presented in Supplementary Note 3 to obtain a calibrated acousto-dielectric field function $\Psi_c(x)$.

To measure the acousto-mechanical and electrical properties of cells, it is necessary to ensure that the cells are subjected to a negative DEP forces in the frequency range of 0.1-20 MHz, so we utilized Tweezing buffer B, which has a higher conductivity, to measure the acousto-mechanical and electrical properties of cells in the experiments. To ensure that the change in buffer conductivity do not interfere with the acoustic-dielectric factor measurement experiments, we fabricated an acousto-dielectric chip with the same design and used polystyrene microparticles suspended in Tweezing buffer B to calibrate the acoustic and electric fields of the chip again. Calibration experiments followed the same steps outlined above. SAWs were excited by IDTs with a 30 Vpp input signal at 7.86 MHz; the AC electric

field was generated by tri-port electrodes with a 7 Vpp signal at 100 kHz. The corresponding measured SAW-induced velocities v_{psl-a} and DEP-induced velocities v_{psl-e} are shown in Fig. S2d and S2e, respectively. The acousto-dielectric field function $\Psi_{cl}(x)$ calibration curve of Tweezer buffer B in Fig. S2f shows similar trends and values to the calibration curve of Tweezer buffer A in Fig. S2c.

2.4. Procedures for measuring acousto-dielectric factors of cells

Once calibrated, our acousto-dielectric chip was used to measure the acousto-dielectric factors of cells. Before conducting experiments, cell solutions (concentration: ~1×10⁶ ml⁻¹) were prepared by resuspending harvested cells in our previously prepared Tweezing buffer A. For our device with a small microfluidic channel (width: 500 μm , height: 40 μm), cell concentrations lower than 10^7 ml⁻¹ were preferred. During each experiment, a cell solution was pumped into the microchannel with a flow rate of 0.2 µL/min to form the center flow, while a buffer without cells was pumped into the microchannel with a flow rate of 0.4 μ L/min to form the sheath flows. The excitation voltage V_a and frequency f_a for the IDTs were set to 30 Vpp and 7.86 MHz. The input voltage V_e and frequency f_e for applying the DEP forces were set to 7 Vpp and 30 kHz. The IDTs and DEP electrodes were located in the area outside the cell membrane. As each cell flowed through the microchannel, under both the acoustic radiation and DEP forces, its lateral position gradually shifted to the equi-acousto-dielectric position and became stable near the channel outlet. In addition to in-plane force components to laterally move cells to equi-acoustodielectric positions, the cells were subjected to vertical force components, which pushed them to the same plane (i.e., the ceiling of a microfluidic channel with a height of 40 µm). A microscope camera was used to record videos of the cell flow (see Supplementary Movie 1) near the channel outlet. From the recorded videos, we extracted the equi-acousto-dielectric positions of the cells, denoted as $x_{equi,n}$ (n =1, 2, 3, ..., N), where n and N represent the event index and total event number. Then, the acoustodielectric factor Φ_n of each captured cell was determined by finding the corresponding value at x = $x_{equi,n}$ from the calibrated acousto-dielectric field function $\Psi_c(x)$.

2.5. Procedures for measuring acousto-mechanical and electrical properties of cells

Biophysical properties such as acoustic (acoustic contrast factor, acoustic impedance, and wave speed), electric (impedance, membrane capacitance, and cytoplasm conductivity), optical (refractive index, scattering, and absorption coefficients), and mechanical (creep compliance, elastic, and viscous modulus) properties have garnered increasing attention in recent years because they are valuable indications for characterizing cell states and functions. Among these parameters, the acoustic contrast factor is also considered as an acousto-mechanical property (Augustsson et al. 2016), as it depends on the cell density and compressibility. Our method uses the acousto-dielectric chip to measure the cells' acousto-mechanical (e.g., acoustic contrast factor) and electrical properties (membrane capacitance and cytoplasm conductivity). Before the experiments, cell solutions (concentration: ~1×10⁶ ml⁻¹) were prepared by suspending cells in our prepared Tweezing buffer B. During our experiments, the excitation voltage V_a and frequency f_a for generating SAWs were set to 30 Vpp and 7.86 MHz. The input voltage V_e for the tri-port electrodes was kept at 7 Vpp; however, a series of DEP frequencies denoted as $[f_{e,m}]_M$ were used. These frequencies ranged from 0.1 to 0.9 MHz with a step of 0.1 MHz and from 1 to 20 MHz with a step of 1 MHz. At individual DEP frequencies, we measured the corresponding equi-acoustodielectric positions $[x_{equi,m}]_M$ and further determined the corresponding acousto-dielectric factors $[\Phi_m]_M$ from the calibration curve of tweezer buffer B. Then, the measured factors at multiple frequencies were used to find a theoretical $\ln |\Phi| - f_e$ curve that best fit the measured factors. The biophysical properties (e.g., acoustic contrast factor, membrane capacitance, and cytoplasm conductivity) corresponding to the identified theoretical curve were considered as the cell's properties determined by our approach. For each cell type, 50 cells were characterized.

2.6. Numerical simulations

To investigate the standing SAW field generated by the IDTs, the resulting acoustic radiation force field, the AC electric field generated by the tri-port electrodes, and the resulting DEP force field, finite element

simulations were performed using the commercial finite element software COMSOL Multiphysics. In particular, the frequency-domain analysis was utilized. A 2D cross-sectional (*x-z* plane) model of our acousto-dielectric chip was established (Fig. S6a). In our model, the substrate (0.5 mm thick Y128-cut LiNbO₃ wafer) was built with the piezoelectric module. The liquid layer (40 µm thick) considered both acoustic pressure and electric current physics (Chen et al. 2018; Chen et al. 2017). The top and side boundaries of the liquid layer were set to impedance conditions matching the impedance (1.04 MPa s m⁻¹) of the polydimethylsiloxane-based microchannel wall (Collins et al. 2016). The substrate-liquid interface was set to an acoustic-structure boundary that coupled the normal pressure.

To simulate SAW generation in the substrate, as well as pressure acoustic waves in the fluid domain, harmonic voltage excitation signals with a frequency f_a of 7.99 MHz were applied to the interdigital electrodes of two IDTs (Delsing et al. 2019). To reduce end reflections of SAWs, perfectly matched layers were added to the left and right ends of the area of interest (Tian et al. 2020). The simulated energy field in the piezoelectric substrate is shown in Fig. S6b, which clearly shows generated Rayleigh-mode, standing SAWs with an antinode at the substrate center. The simulated acoustic energy field and acoustic radiation force distribution in the fluid domain are given in Fig. 1b. On the other hand, to simulate the generated AC electric field in the fluid domain, harmonic voltage signals with a frequency f_e of 30 kHz were applied to the tri-port electrodes. The simulated electric energy field and the DEP force distribution in the fluid domain are given in Fig. 1c.

3. Results and discussion

3.1. Mechanism of acousto-dielectric tweezers

The acousto-dielectric tweezers utilize the balance between acoustic radiation and DEP forces applied on individual cells. Fig. 1a displays a device schematic for acousto-dielectric tweezers (see Fig. S1 for a photo). The device is composed of a pair of IDTs deposited on a LiNbO₃ substrate to generate standing

SAWs and apply acoustic radiation forces **F**_{ARF} on cells flowing through a polydimethylsiloxane-based microchannel (Guo et al. 2015). The device also contains parallel tri-port electrodes within the microchannel to generate AC electric fields and apply controlled DEP forces **F**_{DEP} on the cells (Albrecht et al. 2004). Particularly, the microchannel, IDTs, and tri-port electrodes are all arranged symmetrically with respect to the device's centerline. With this configuration, a generated acoustic antinode line coincides with both the microchannel and the tri-port electrodes' centerlines. Moreover, the microchannel width is close to a wavelength, meaning only two acoustic node lines can be generated in the microchannel as illustrated in Fig. 1a.

When only standing SAWs at a frequency of f_a are generated from the IDTs, the cells or microparticles loaded in the microchannel will experience x-component acoustic radiation forces F_{ARF-x} . Accordingly, the cells or microparticles with positive acoustic contrast factors will be moved to the acoustic pressure nodes, as shown in our numerical (Fig. 1b) and experimental (Fig. 1d, left) results. Here, positive acoustic contrast factors for cells can be achieved by adjusting the cell buffer properties (e.g., density and acoustic impedance) (Baudoin et al. 2019). On the other hand, when only an AC electric field with a frequency of f_e is generated by the tri-port electrodes, cells or microparticles in the dynamic electric field will experience x-component DEP forces F_{DEP-x} , which are highly dependent on the Clausius-Mossotti factor (Kim et al. 2019). This study employs negative DEP forces to move cells to the microchannel's centerline with weak local electric field intensities, as indicated by our numerical (Fig. 1c) and experimental (Fig. 1d, middle) results. Note that positive DEP forces typically attract cells to positions with strong local electric field intensities, which may damage the cells (D'Amico et al. 2017). For a given cell type, negative DEP forces can be achieved by adjusting the AC electric field frequency f_e and the cell buffer's conductivity, since the Clausius-Mossotti factor highly relies on these two factors in addition to other cell properties (Elitas et al. 2014).

When standing SAWs and an AC electric field are generated simultaneously, a cell or microparticle in the device's microchannel is subjected to both acoustic radiation and DEP forces, which vary spatially

as shown in Fig. 1b and 1c. Therefore, the cell or microparticle in the microchannel should be translated to an equilibrium position x_{equi} , where the x-component acoustic radiation and DEP forces have the same magnitude but in opposite directions, *i.e.*, F_{AFR-x} (x_{equi}) = $-F_{DEP-x}$ (x_{equi}). As shown in the microscopy image (Fig. 1d, right), polystyrene microparticles were trapped at equi-acousto-dielectric positions, which are between the center trapping region (*i.e.*, the microchannel centerline) at the condition with only an AC electric field and the side trapping regions (*i.e.*, pressure node lines) at the condition with only standing SAWs. Moreover, by increasing the input voltage for generating an AC electric field, microparticles originally trapped at the acoustic pressure nodes can be gradually moved to the center of the microchannel, as illustrated in Fig. 1e and 1f. This observation demonstrates the change in equilibrium position when increasing the DEP forces. In addition to the device design in Fig. 1, other designs that allow for generating acoustic radiation and DEP forces in counter directions may also trap microparticles at equi-acousto-dielectric positions. To predict the manipulation process for our acousto-dielectric tweezers, a theoretical model was established by considering the SAW-induced acoustic radiation force and the AC electric field-induced DEP force on a cell (Supplementary Note 1).

3.2. Acousto-dielectric factor and acousto-dielectric field function

Through a theoretical study (Supplementary Note 3), we discovered that the equi-acousto-dielectric position x_{equi} is correlated to the ratio $\varphi_a/\text{Re}(\gamma_{CM})$, where φ_a and $\text{Re}(\gamma_{CM})$ represent the acoustic contrast factor and the real part of the Clausius-Mossotti factor, respectively. Here, the ratio $\varphi_a/\text{Re}(\gamma_{CM})$ is defined as a dimensionless parameter Φ (namely, acousto-dielectric factor), which depends on the DEP frequency as well as the cell's acoustic and electrical properties. Primarily, our theoretical study revealed that the acousto-dielectric factor gradually approaches $-2\varphi_a$ as the DEP frequency is decreased, while the acousto-dielectric factor gradually approaches $\varphi_a(\sigma_{cyto}+2\sigma_b)/(\sigma_{cyto}-\sigma_b)$ as the DEP frequency is increased. In addition, we theoretically investigated the individual effects of cell properties (including the acoustic contrast factor φ_a , cell density ρ_c , cell compressibility κ_c , buffer conductivity σ_b , cytoplasm

conductivity σ_{cyto} , membrane capacitance C_{mem} , and cell radius R) on the acousto-dielectric factor. Based on the theoretical curves (e.g., $\ln |\Phi|$ versus f_e) plotted in Fig. 2b-2h, the following relationships were established. (i) Increasing acoustic contrast factors results in higher acousto-dielectric factors for frequencies ranging from 0.01 to 20 MHz (Fig. 2b). Because cell compressibility and density have a significant impact on the acoustic contrast factor (Eq. S3), variations of these properties also result in higher acousto-dielectric factors within the aforementioned frequency range (Fig. 2g and 2h). (ii) Increasing cytoplasm conductivities causes higher acousto-dielectric factors in the frequency range above 1 MHz, while acousto-dielectric factors in the frequency range below 1 MHz did not change considerably (Fig. 2c). (iii) Changes of membrane capacitances and cell radii primarily affect the acousto-dielectric factors in the mid-frequency range (0.1-10 MHz) and have a minimal effect on the acousto-dielectric factors in lower and higher frequency regions (Fig. 2d and 2e). (iv) Increased buffer conductivities lead to higher acousto-dielectric factors in the frequency range above 0.1 MHz (Fig. 2f). Moreover, because the acousto-dielectric factor relies heavily on the object's acoustic and electrical properties, different types of objects (such as polystyrene particles, HeLa cells, and MCF7 cells with the same radius) should theoretically have different acousto-dielectric factors, as shown in Fig. 2i. This result suggests that the acousto-dielectric factor can be used to classify various cell types of similar sizes with different biophysical properties.

Our theoretical study (Supplementary Note 2) reveals that the acousto-dielectric factor Φ is equal to the value of an acousto-dielectric field function $\Psi(x)$ at the equi-acousto-dielectric position x_{equi} . This field function $\Psi(x)$ depends on the acoustic potential field, the electric potential field, and the buffer properties. Hence, once the device configuration, buffer properties, and operation parameters are determined, the field function can be experimentally calibrated. To obtain a calibrated field function $\Psi_c(x)$, we considered a scenario where solely standing SAWs at a frequency f_a were generated by the IDTs. The SAW-induced velocities v_{ps-a} of the polystyrene particles (Fig. S2a) were measured by tracking and analyzing changes in the position of the particle recorded by a microscope camera. We also

measured the DEP-induced velocities v_{ps-e} of polystyrene particles (Fig. S2b) when only an AC electric field was generated by the tri-port electrodes. Based on the measured particle velocities, as well as the known material properties of the buffer and polystyrene particles, a calibrated acousto-dielectric field function $\Psi_c(x)$ was obtained using the equations in Supplementary Note 3. The calibrated function $\Psi_c(x)$ monotonically increases with an increase of x when x > 0 (or with a decrease of x when x < 0), as shown in Fig. S2c. Therefore, by using our acousto-dielectric device, it is feasible to quantitatively measure the acousto-dielectric factor Φ of a cell flowing through our device, by tracking the cell's equilibrium position x_{equi} in our device and then finding the corresponding value at the position x_{equi} using the calibrated acousto-dielectric field function $\Psi_c(x)$.

3.3. Characterizing acousto-dielectric factors of cells

Because the acousto-dielectric factor primarily depends on the cell's acoustic and electrical properties and is minimally affected by the cell radius at low and high electric field frequencies (Fig. 2b-2h), this factor holds significant potential for cell characterization and size-insensitive cell phenotyping. Our experimental procedures for measuring the acousto-dielectric factor are illustrated in Fig. 3a. Cells stained with calcein AM were suspended in a buffer and then loaded into the microchannel with both standing SAW and AC electric fields. As the n^{th} cell flows through the microchannel, it gradually moves to the equi-acousto-dielectric position $x_{equi,n}$, which can be measured using a captured microscopy image. Since the entire device is symmetrical with respect to the microchannel's center, cells with the same properties may stay at two equi-acousto-dielectric positions ($\pm x_{equi}$) as shown Fig. 3a (inset). Then, the n^{th} cell's acousto-dielectric factor Φ_n can further be determined, by finding the value of the calibrated acousto-dielectric field function $\Psi_c(x)$ at the equi-acousto-dielectric position $x_{equi,n}$, *i.e.*, $\Phi_n = \Psi_c(x = x_{equi,n})$.

Experiments were performed to measure acousto-dielectric factors for 293T, HeLa, and Jurkat cells using our acousto-dielectric chip with 7.86 MHz SAWs and a 30 kHz AC electric field. The measured

acousto-dielectric factors for 293T cells (two experiments: n = 821 and 514) versus event indices are plotted in Fig. 3b. The slopes of the linear least-square fitting results are small, indicating relatively low data drifting and good time stability across measurements. In fact, both acoustic radiation forces and DEP were used to manipulate living cells and showed great biocompatibility in the previous studies (Guo et al. 2016; Kim et al. 2019). The scatter plots in Fig. 3c show that the acousto-dielectric factors measured for 293T, HeLa, and Jurkat cells have different distributions. Moreover, the comparison in Fig. 3d shows that the equi-acousto-dielectric positions x_{equi} for HeLa and 293T cells are spatially distributed in two different regions even though these two types of cells have highly overlapping size distributions (Fig. S3). This result implies that our approach based on equi-acousto-dielectric positions can potentially be used to spatially separate two cell populations with overlapping size distributions. Furthermore, the scatter plots of the acousto-dielectric factors versus cell diameters (Fig. 3e) for Jurkat and 293T cells are distributed in different clusters.

3.4. Characterizing acousto-mechanical and electrical properties of cells

The findings of our theoretical study indicate that different cell properties lead to distinct relations between acousto-dielectric factors and applied AC electric field frequencies. As shown in Fig. 2, the acoustic contrast factor, which depends on the cell density and compressibility, significantly affects the acousto-dielectric factor in a wide AC electric field frequency range (*e.g.*, 0.01 – 20 MHz). The acousto-dielectric factor and cytoplasm conductivity are highly correlated in the high-frequency range (*e.g.*, >1 MHz). Different membrane capacitances lead to noticeable changes in acousto-dielectric factors within the mid-frequency range (*e.g.*, 0.1 to 1 MHz). Therefore, if acousto-dielectric factors in a wide frequency range can be experimentally measured, it will become feasible to inversely determine the acoustic and electrical properties of cells.

Based on the acousto-dielectric tweezing mechanism, we established an approach to quantitatively characterize the acoustic contrast factor, cytoplasm conductivity, and membrane capacitance. Fig. 4a

illustrates the key steps of this approach. Initially, the equi-acousto-dielectric positions $[x_{equi,m}]_M$ of a cell loaded in a microchannel are measured at conditions with different DEP frequencies $[f_{e,m}]_M$ (frequency index $m = 1, 2, \dots M$). As shown in Fig. 4b, by increasing the applied DEP frequency, the equi-acousto-dielectric position of a HeLa cell gradually moves away from the center of the channel. Next, the acousto-dielectric factors $[\Phi_m]_M$ corresponding to the measured equi-acousto-dielectric positions $[x_{equi,m}]_M$ are determined, by referring to the calibrated acousto-dielectric field function $\Psi_{cl}(x)$. Lastly, a theoretical curve (i.e., $\ln|\Phi| - f_e$ relation) that best fits the experimentally determined acousto-dielectric factors at multiple frequencies can be found. The properties (e.g., acoustic contrast factor, membrane capacitance, and cytoplasm conductivity) corresponding to the identified theoretical curve are considered to be the target cell's properties quantitatively characterized by our approach.

To validate our approach, experiments were performed using Jurkat, HeLa, 293T, and MCF7 cells. The measured $\ln|\Phi| - f_e$ relations are shown in Fig. 4c (left to right: Jurkat, HeLa, 293T, and MCF7 cells). Fig. 4d-f are scatter plots of quantitatively characterized acoustic contrast factors, membrane capacitances, and cytoplasm conductivities, respectively. By comparing the characterized cell properties among different cell types, it can be found that the acoustic contrast factors φ_a for the four cell types have dissimilar distributions with the HeLa cell population having the highest median φ_a (Fig. 4d). The distributions of cytoplasm conductivities σ_{cyto} for the four cell types also show different distributions with the 293T cell group having the highest median σ_{cyto} (Fig. 4f). In contrast, the membrane capacitance C_{mem} distributions for the four cell types only have slight differences (Fig. 4e). The cell properties characterized by our approach are consistent with values found in the literatures (Gentet et al. 2000; Suresh 2007; Weiss et al. 2007; Xie et al. 2016; Zhang et al. 2020). However, none of the previous single-cell biophysical analysis methods could characterize both acoustic contrast factors and electrical properties of cells. The results in Fig. 4 demonstrate the capability of our method for characterizing

different types of cells. In the future, we will investigate the capability of our method for characterizing cells at different states, such as live/dead and resting/dividing cells.

4. Conclusions

In this study, we established an acousto-dielectric tweezing mechanism for size-insensitive manipulation and biophysical characterization of single cells. To perform acousto-dielectric tweezing, we developed an acousto-dielectric device, which employs a pair of IDTs on a LiNbO₃ wafer in order to generate controlled standing SAWs and apply acoustic radiation forces on the cells. The acousto-dielectric device also contains tri-port electrodes in order to generate controlled AC electric fields and apply DEP forces on the cells. When cells experience the standing SAW and AC electric fields, our tweezing mechanism traps cells at equi-acousto-dielectric positions x_{equi} , where the cells are subjected to the balanced acoustic radiation and DEP forces, i.e., $F_{AFR-x}(x_{equi}) = -F_{DEP-x}(x_{equi})$. Interestingly, at various SAW and AC electric field conditions, our theoretical and experimental results revealed that the equi-acousto-dielectric positions x_{equi} are insensitive to cell volumes and primarily affected by cell-intrinsic biophysical properties. These biophysical properties include the membrane capacitance, cytoplasm conductivity, and acoustic contrast factor, which depends on both the cell density and the cell compressibility. Due to this feature, our acousto-dielectric tweezing mechanism is a valuable tool for separating cell populations with overlapping sizes, analyzing single-cell biophysical properties, as well as providing an additional biophysical property-based indicator for cell phenotyping.

To validate our acousto-dielectric tweezing mechanism and demonstrate its potential functions, we performed proof-of-concept experiments using an acousto-dielectric chip with a pair of IDTs, tri-port electrodes, and a microfluidic channel. Our experimental results in Fig. 3d shows that HeLa and 293T cells (*i.e.*, cells with overlapping size distributions) were trapped at different equi-acousto-dielectric positions because of their differing biophysical properties. We expect our mechanism to assist in the development of future size-insensitive cell separation technologies that are primarily based on cell-

intrinsic biophysical properties. Our experimental results in Fig. 3e demonstrate that the acousto-dielectric factor measured by our approach has the potential to provide a supplementary biophysical property-based indicator for cell phenotyping. In addition, our experimental results (Fig. 4) show that the acousto-dielectric factors measured at various AC electric field frequencies can inversely determine multiple biophysical properties, including membrane capacitance, cytoplasm conductivity, and acoustic contrast factor, which is correlated to the cell density and the cell compressibility. Although our method enables the aforementioned functions, it is limited to measuring the acoustic contrast factor, cytoplasm conductivity, and membrane capacitance. For measuring the acousto-dielectric factor, the throughput observed in our experiments was 328 cells/min with a standard deviation of 102 cells/min. To increase the throughput, we plan to increase the flow rate, increase the camera's frame rate, increase the cell concentration, as well as integrate multiple acousto-dielectric tweezing units. In the long run, we expect the acousto-dielectric tweezing mechanism will spur the development of future platforms for high-throughput analysis of single-cell biophysical properties in biological and medical research.

Acknowledgements

This work was partly supported by the National Science Foundation (CMMI-2104526) and the National Natural Science Foundation of China (Grant No. 52175545). This material was based upon work supported by the National Science Foundation Graduate Research Fellowship under Grant No. 1644868.

Credit author statement: Z.T. and L.S. conceived the idea. L.S. developed the models for simulations. L.S. designed, fabricated, and characterized acousto-dielectric devices. J.Z., H.Z., and K.Y. fabricated the acousto-dielectric devices. L.S., N.H., Z.P., G.J., and Y.L. conducted the experiments. L.S. analyzed the data. Z.T., L.S., T.L., S.Y., J.R., N.U., W.C. and T.J.H. wrote the paper. W.C. and T.J.H. supervised the study.

Conflicts of interests: T.J.H. has co-founded a start-up company, Ascent Bio-Nano Technologies Inc., to commercialize technologies involving acoustofluidics and acoustic tweezers. All other authors declare no competing interests.

Data availability: The authors declare that all data supporting the findings of this study are available within the article and the supplementary materials. Further information is available from the corresponding author upon reasonable request.

References

- Actis, P., Tokar, S., Clausmeyer, J., Babakinejad, B., Mikhaleva, S., Cornut, R., Takahashi, Y., López Córdoba, A., Novak, P., Shevchuck, A.I., Dougan, J.A., Kazarian, S.G., Gorelkin, P.V., Erofeev, A.S., Yaminsky, I.V., Unwin, P.R., Schuhmann, W., Klenerman, D., Rusakov, D.A., Sviderskaya, E.V., Korchev, Y.E., 2014. Electrochemical Nanoprobes for Single-Cell Analysis. ACS Nano 8(1), 875-884.
- Ahmed, D., Baasch, T., Blondel, N., Läubli, N., Dual, J., Nelson, B.J., 2017. Neutrophil-inspired propulsion in a combined acoustic and magnetic field. Nat. Commun 8(1), 770.
- Albrecht, D.R., Sah, R.L., Bhatia, S.N., 2004. Geometric and Material Determinants of Patterning Efficiency by Dielectrophoresis. Biophys. J. 87(4), 2131-2147.
- Alcaraz, J., Buscemi, L., Grabulosa, M., Trepat, X., Fabry, B., Farré, R., Navajas, D., 2003. Microrheology of Human Lung Epithelial Cells Measured by Atomic Force Microscopy. Biophys. J. 84(3), 2071-2079.
- Augustsson, P., Karlsen, J.T., Su, H.-W., Bruus, H., Voldman, J., 2016. Iso-acoustic focusing of cells for size-insensitive acousto-mechanical phenotyping. Nat. Commun 7(1), 11556.
- Baudoin, M., Gerbedoen, J.-C., Riaud, A., Matar Olivier, B., Smagin, N., Thomas, J.-L., 2019. Folding a focalized acoustical vortex on a flat holographic transducer: Miniaturized selective acoustical tweezers. Sci. Adv. 5(4), eaav1967.
- Baudoin, M., Thomas, J.-L., Sahely, R.A., Gerbedoen, J.-C., Gong, Z., Sivery, A., Matar, O.B., Smagin, N., Favreau, P., Vlandas, A., 2020. Spatially selective manipulation of cells with single-beam acoustical tweezers. Nat. Commun 11(1), 4244.
- Bernassau, A.L., MacPherson, P.G.A., Beeley, J., Drinkwater, B.W., Cumming, D.R.S., 2013. Patterning of microspheres and microbubbles in an acoustic tweezers. Biomed. Microdevices 15(2), 289-297.
- Bruus, H., 2012. Acoustofluidics 7: The acoustic radiation force on small particles. Lab Chip 12(6), 1014-1021.
- Chen, C., Gu, Y., Philippe, J., Zhang, P., Bachman, H., Zhang, J., Mai, J., Rufo, J., Rawls, J.F., Davis, E.E., Katsanis, N., Huang, T.J., 2021. Acoustofluidic rotational tweezing enables high-speed contactless morphological phenotyping of zebrafish larvae. Nat. Commun 12(1), 1118.
- Chen, C., Zhang, S.P., Mao, Z., Nama, N., Gu, Y., Huang, P.-H., Jing, Y., Guo, X., Costanzo, F., Huang, T.J., 2018. Three-dimensional numerical simulation and experimental investigation of boundary-driven streaming in surface acoustic wave microfluidics. Lab Chip 18(23), 3645-3654.
- Chen, X., Ren, Y., Liu, W., Feng, X., Jia, Y., Tao, Y., Jiang, H., 2017. A Simplified Microfluidic Device for Particle Separation with Two Consecutive Steps: Induced Charge Electro-osmotic Prefocusing and Dielectrophoretic Separation. Anal. Chem. 89(17), 9583-9592.
- Chen, Y., Ding, X., Steven Lin, S.-C., Yang, S., Huang, P.-H., Nama, N., Zhao, Y., Nawaz, A.A., Guo, F., Wang, W., Gu, Y., Mallouk, T.E., Huang, T.J., 2013. Tunable Nanowire Patterning Using Standing Surface Acoustic Waves. ACS Nano 7(4), 3306-3314.
- Chung, B.G., Manbachi, A., Khademhosseini, A., 2007. A Microfluidic Device with Groove Patterns for Studying Cellular Behavior. JoVE(7), e270.
- Collins, D.J., Devendran, C., Ma, Z., Ng Jia, W., Neild, A., Ai, Y., 2016. Acoustic tweezers via subtime-of-flight regime surface acoustic waves. Sci. Adv. 2(7), e1600089.

- D'Amico, L., Ajami, N.J., Adachi, J.A., Gascoyne, P.R.C., Petrosino, J.F., 2017. Isolation and concentration of bacteria from blood using microfluidic membraneless dialysis and dielectrophoresis. Lab Chip 17(7), 1340-1348.
- Delsing, P., Cleland, A.N., Schuetz, M.J.A., Knörzer, J., Giedke, G., Cirac, J.I., Srinivasan, K., Wu, M., Balram, K.C., Bäuerle, C., Meunier, T., Ford, C.J.B., Santos, P.V., Cerda-Méndez, E., Wang, H., Krenner, H.J., Nysten, E.D.S., Weiß, M., Nash, G.R., Thevenard, L., Gourdon, C., Rovillain, P., Marangolo, M., Duquesne, J.-Y., Fischerauer, G., Ruile, W., Reiner, A., Paschke, B., Denysenko, D., Volkmer, D., Wixforth, A., Bruus, H., Wiklund, M., Reboud, J., Cooper, J.M., Fu, Y., Brugger, M.S., Rehfeldt, F., Westerhausen, C., 2019. The 2019 surface acoustic waves roadmap. J. Phys. D 52(35), 353001.
- Destgeer, G., Sung, H.J., 2015. Recent advances in microfluidic actuation and micro-object manipulation via surface acoustic waves. Lab Chip 15(13), 2722-2738.
- Durmus, N.G., Tekin, H.C., Guven, S., Sridhar, K., Arslan Yildiz, A., Calibasi, G., Ghiran, I., Davis, R.W., Steinmetz, L.M., Demirci, U., 2015. Magnetic levitation of single cells. Proc. Natl. Acad. Sci. 112(28), E3661.
- Elitas, M., Martinez-Duarte, R., Dhar, N., McKinney, J.D., Renaud, P., 2014. Dielectrophoresis-based purification of antibiotic-treated bacterial subpopulations. Lab Chip 14(11), 1850-1857.
- Fregin, B., Czerwinski, F., Biedenweg, D., Girardo, S., Gross, S., Aurich, K., Otto, O., 2019. High-throughput single-cell rheology in complex samples by dynamic real-time deformability cytometry. Nat. Commun 10(1), 415.
- Gentet, L.J., Stuart, G.J., Clements, J.D., 2000. Direct Measurement of Specific Membrane Capacitance in Neurons. Biophys. J. 79(1), 314-320.
- Gossett, D.R., Tse, H.T.K., Lee, S.A., Ying, Y., Lindgren, A.G., Yang, O.O., Rao, J., Clark, A.T., Di Carlo, D., 2012. Hydrodynamic stretching of single cells for large population mechanical phenotyping. Proc. Natl. Acad. Sci. 109(20), 7630-7635.
- Guo, F., Li, P., French, J.B., Mao, Z., Zhao, H., Li, S., Nama, N., Fick, J.R., Benkovic, S.J., Huang, T.J., 2015. Controlling cell-cell interactions using surface acoustic waves. Proc. Natl. Acad. Sci. 112(1), 43.
- Guo, F., Mao, Z., Chen, Y., Xie, Z., Lata James, P., Li, P., Ren, L., Liu, J., Yang, J., Dao, M., Suresh, S., Huang Tony, J., 2016. Three-dimensional manipulation of single cells using surface acoustic waves. Proc. Natl. Acad. Sci. 113(6), 1522-1527.
- Guo, Q., Park, S., Ma, H., 2012. Microfluidic micropipette aspiration for measuring the deformability of single cells. Lab Chip 12(15), 2687-2695.
- Guo, X., Sun, M., Yang, Y., Xu, H., Liu, J., He, S., Wang, Y., Xu, L., Pang, W., Duan, X., 2021. Controllable Cell Deformation Using Acoustic Streaming for Membrane Permeability Modulation. Adv. Sci. 8(3), 2002489.
- Hao, N., Wang, Z., Liu, P., Becker, R., Yang, S., Yang, K., Pei, Z., Zhang, P., Xia, J., Shen, L., Wang, L., Welsh-Bohmer, K.A., Sanders, L., Lee, L.P., Huang, T.J., 2022. Acoustofluidic multimodal diagnostic system for Alzheimer's disease. Biosens. Bioelectron. 196, 113730.
- Harada, Y., Asakura, T., 1996. Radiation forces on a dielectric sphere in the Rayleigh scattering regime. Opt. Commun. 124(5), 529-541.
- Hochmuth, R.M., 2000. Micropipette aspiration of living cells. J. Biomech. 33(1), 15-22.

- Hwang, J.Y., Kim, J., Park, J.M., Lee, C., Jung, H., Lee, J., Shung, K.K., 2016. Cell Deformation by Single-beam Acoustic Trapping: A Promising Tool for Measurements of Cell Mechanics. Sci. Rep. 6(1), 27238.
- Kim, D., Sonker, M., Ros, A., 2019. Dielectrophoresis: From Molecular to Micrometer-Scale Analytes. Anal. Chem. 91(1), 277-295.
- Koch, M., Wright, K.E., Otto, O., Herbig, M., Salinas, N.D., Tolia, N.H., Satchwell, T.J., Guck, J., Brooks, N.J., Baum, J., 2017. Plasmodium falciparum erythrocyte-binding antigen 175 triggers a biophysical change in the red blood cell that facilitates invasion. Proc. Natl. Acad. Sci. 114(16), 4225.
- Kooiman, K., Vos, H.J., Versluis, M., de Jong, N., 2014. Acoustic behavior of microbubbles and implications for drug delivery. Adv. Drug Del. Rev. 72, 28-48.
- Kuznetsova, T.G., Starodubtseva, M.N., Yegorenkov, N.I., Chizhik, S.A., Zhdanov, R.I., 2007. Atomic force microscopy probing of cell elasticity. Micron 38(8), 824-833.
- Lange, Janina R., Steinwachs, J., Kolb, T., Lautscham, Lena A., Harder, I., Whyte, G., Fabry, B., 2015. Microconstriction Arrays for High-Throughput Quantitative Measurements of Cell Mechanical Properties. Biophys. J. 109(1), 26-34.
- Laurell, T., Petersson, F., Nilsson, A., 2007. Chip integrated strategies for acoustic separation and manipulation of cells and particles. Chem. Soc. Rev. 36(3), 492-506.
- Lautenschläger, F., Paschke, S., Schinkinger, S., Bruel, A., Beil, M., Guck, J., 2009. The regulatory role of cell mechanics for migration of differentiating myeloid cells. Proc. Natl. Acad. Sci. 106(37), 15696.
- Liang, S., Chaohui, W., Qiao, H., 2018. Force on a compressible sphere and the resonance of a bubble in standing surface acoustic waves. Phys. Rev. E 98(4), 043108.
- Lin, S.-C.S., Mao, X., Huang, T.J., 2012. Surface acoustic wave (SAW) acoustophoresis: now and beyond. Lab Chip 12(16), 2766-2770.
- Lipfert, J., Hao, X., Dekker, N.H., 2009. Quantitative Modeling and Optimization of Magnetic Tweezers. Biophys. J. 96(12), 5040-5049.
- Loo, J.F.-C., Ho, H.P., Kong, S.K., Wang, T.-H., Ho, Y.-P., 2019. Technological Advances in Multiscale Analysis of Single Cells in Biomedicine. Adv. Biosyst. 3(11), 1900138.
- Ma, Z., Holle, A.W., Melde, K., Qiu, T., Poeppel, K., Kadiri, V.M., Fischer, P., 2020. Acoustic Holographic Cell Patterning in a Biocompatible Hydrogel. Adv. Mater. 32(4), 1904181.
- Maloney, J.M., Nikova, D., Lautenschläger, F., Clarke, E., Langer, R., Guck, J., Van Vliet, K.J., 2010. Mesenchymal Stem Cell Mechanics from the Attached to the Suspended State. Biophys. J. 99(8), 2479-2487.
- Mei, J., Zhang, N., Friend, J., 2020. Fabrication of Surface Acoustic Wave Devices on Lithium Niobate. JoVE(160), e61013.
- Mills, J.P., Qie, L., Dao, M., Lim, C.T., Suresh, S., 2004. Nonlinear elastic and viscoelastic deformation of the human red blood cell with optical tweezers. Mech. Chem. Biosyst. 1(3), 169-180.
- Mishra, P., Hill, M., Glynne-Jones, P., 2014. Deformation of red blood cells using acoustic radiation forces. Biomicrofluidics 8(3), 034109.
- Mugnano, M., Memmolo, P., Miccio, L., Merola, F., Bianco, V., Bramanti, A., Gambale, A., Russo, R.,

- Andolfo, I., Iolascon, A., Ferraro, P., 2018. Label-Free Optical Marker for Red-Blood-Cell Phenotyping of Inherited Anemias. Anal. Chem. 90(12), 7495-7501.
- Munder, M.C., Midtvedt, D., Franzmann, T., Nuske, E., Otto, O., Herbig, M., Ulbricht, E., Müller, P., Taubenberger, A., Maharana, S., 2016. A pH-driven transition of the cytoplasm from a fluid-to a solid-like state promotes entry into dormancy. Elife 5, e09347.
- Nyberg, K.D., Hu, K.H., Kleinman, S.H., Khismatullin, D.B., Butte, M.J., Rowat, A.C., 2017. Quantitative Deformability Cytometry: Rapid, Calibrated Measurements of Cell Mechanical Properties. Biophys. J. 113(7), 1574-1584.
- Otto, O., Rosendahl, P., Mietke, A., Golfier, S., Herold, C., Klaue, D., Girardo, S., Pagliara, S., Ekpenyong, A., Jacobi, A., Wobus, M., Töpfner, N., Keyser, U.F., Mansfeld, J., Fischer-Friedrich, E., Guck, J., 2015. Real-time deformability cytometry: on-the-fly cell mechanical phenotyping. Nat. Methods 12(3), 199-202.
- Pagliara, S., Franze, K., McClain, C.R., Wylde, G.W., Fisher, C.L., Franklin, R.J.M., Kabla, A.J., Keyser, U.F., Chalut, K.J., 2014. Auxetic nuclei in embryonic stem cells exiting pluripotency. Nat. Mater. 13(6), 638-644.
- Panhwar, M.H., Czerwinski, F., Dabbiru, V.A.S., Komaragiri, Y., Fregin, B., Biedenweg, D., Nestler, P., Pires, R.H., Otto, O., 2020. High-throughput cell and spheroid mechanics in virtual fluidic channels. Nat. Commun 11(1), 2190.
- Pethig, R., 2010. Dielectrophoresis: Status of the theory, technology, and applications. Biomicrofluidics 4(2), 022811.
- Rosendahl, P., Plak, K., Jacobi, A., Kraeter, M., Toepfner, N., Otto, O., Herold, C., Winzi, M., Herbig, M., Ge, Y., Girardo, S., Wagner, K., Baum, B., Guck, J., 2018. Real-time fluorescence and deformability cytometry. Nat. Methods 15(5), 355-358.
- Rufo, J., Cai, F., Friend, J., Wiklund, M., Huang, T.J., 2022a. Acoustofluidics for biomedical applications. Nature Reviews Methods Primers 2(1), 30.
- Rufo, J., Zhang, P., Zhong, R., Lee, L.P., Huang, T.J., 2022b. A sound approach to advancing healthcare systems: the future of biomedical acoustics. Nat. Commun 13(1), 3459.
- Shafiee, H., Caldwell, J.L., Sano, M.B., Davalos, R.V., 2009. Contactless dielectrophoresis: a new technique for cell manipulation. Biomed. Microdevices 11(5), 997.
- Suresh, S., 2007. Biomechanics and biophysics of cancer cells. Acta Materialia 55(12), 3989-4014.
- Tao, R., Hasan, S.A., Wang, H.Z., Zhou, J., Luo, J.T., McHale, G., Gibson, D., Canyelles-Pericas, P., Cooke, M.D., Wood, D., Liu, Y., Wu, Q., Ng, W.P., Franke, T., Fu, Y.Q., 2018. Bimorph material/structure designs for high sensitivity flexible surface acoustic wave temperature sensors. Sci. Rep. 8(1), 9052.
- Tian, Z., Wang, Z., Zhang, P., Naquin Ty, D., Mai, J., Wu, Y., Yang, S., Gu, Y., Bachman, H., Liang, Y., Yu, Z., Huang Tony, J., 2020. Generating multifunctional acoustic tweezers in Petri dishes for contactless, precise manipulation of bioparticles. Sci. Adv. 6(37), eabb0494.
- Tian, Z., Yang, S., Huang, P.-H., Wang, Z., Zhang, P., Gu, Y., Bachman, H., Chen, C., Wu, M., Xie, Y., Huang Tony, J., 2019. Wave number–spiral acoustic tweezers for dynamic and reconfigurable manipulation of particles and cells. Sci. Adv. 5(5), eaau6062.
- Urbanska, M., Muñoz, H.E., Shaw Bagnall, J., Otto, O., Manalis, S.R., Di Carlo, D., Guck, J., 2020. A comparison of microfluidic methods for high-throughput cell deformability measurements. Nat.

- Methods 17(6), 587-593.
- Wang, H., Liu, Z., Shin, D.M., Chen, Z.G., Cho, Y., Kim, Y.-J., Han, A., 2019. A continuous-flow acoustofluidic cytometer for single-cell mechanotyping. Lab Chip 19(3), 387-393.
- Wang, L., Flanagan, L.A., Jeon, N.L., Monuki, E., Lee, A.P., 2007. Dielectrophoresis switching with vertical sidewall electrodes for microfluidic flow cytometry. Lab Chip 7(9), 1114-1120.
- Weiss, E.C., Anastasiadis, P., Pilarczyk, G., Lemor, R.M., Zinin, P.V., 2007. Mechanical Properties of Single Cells by High-Frequency Time-Resolved Acoustic Microscopy. IEEE Trans. Ultrason. Ferroelectr. Freq. Control 54(11), 2257-2271.
- Xie, Y., Nama, N., Li, P., Mao, Z., Huang, P.-H., Zhao, C., Costanzo, F., Huang, T.J., 2016. Probing Cell Deformability via Acoustically Actuated Bubbles. Small 12(7), 902-910.
- Yang, D., Zhou, Y., Zhou, Y., Han, J., Ai, Y., 2019. Biophysical phenotyping of single cells using a differential multiconstriction microfluidic device with self-aligned 3D electrodes. Biosens. Bioelectron. 133, 16-23.
- Yang, S., Tian, Z., Wang, Z., Rufo, J., Li, P., Mai, J., Xia, J., Bachman, H., Huang, P.-H., Wu, M., Chen, C., Lee, L.P., Huang, T.J., 2022. Harmonic acoustics for dynamic and selective particle manipulation. Nat. Mater.
- Yeo, L.Y., Friend, J.R., 2014. Surface Acoustic Wave Microfluidics. Annu. Rev. Fluid Mech. 46(1), 379-406.
- Zhang, L., 2018. From acoustic radiation pressure to three-dimensional acoustic radiation forces. JAMA 144(1), 443-447.
- Zhang, Z., Zheng, T., Zhu, R., 2020. Characterization of single-cell biophysical properties and cell type classification using dielectrophoresis model reduction method. Sens. Actuators B Chem. 304, 127326.
- Zhao, Y., Chen, D., Luo, Y., Li, H., Deng, B., Huang, S.-B., Chiu, T.-K., Wu, M.-H., Long, R., Hu, H., Zhao, X., Yue, W., Wang, J., Chen, J., 2013. A microfluidic system for cell type classification based on cellular size-independent electrical properties. Lab Chip 13(12), 2272-2277.
- Zhao, Y., Jiang, M., Chen, D., Zhao, X., Xue, C., Hao, R., Yue, W., Wang, J., Chen, J., 2016. Single-Cell Electrical Phenotyping Enabling the Classification of Mouse Tumor Samples. Sci. Rep. 6(1), 19487.

Figures

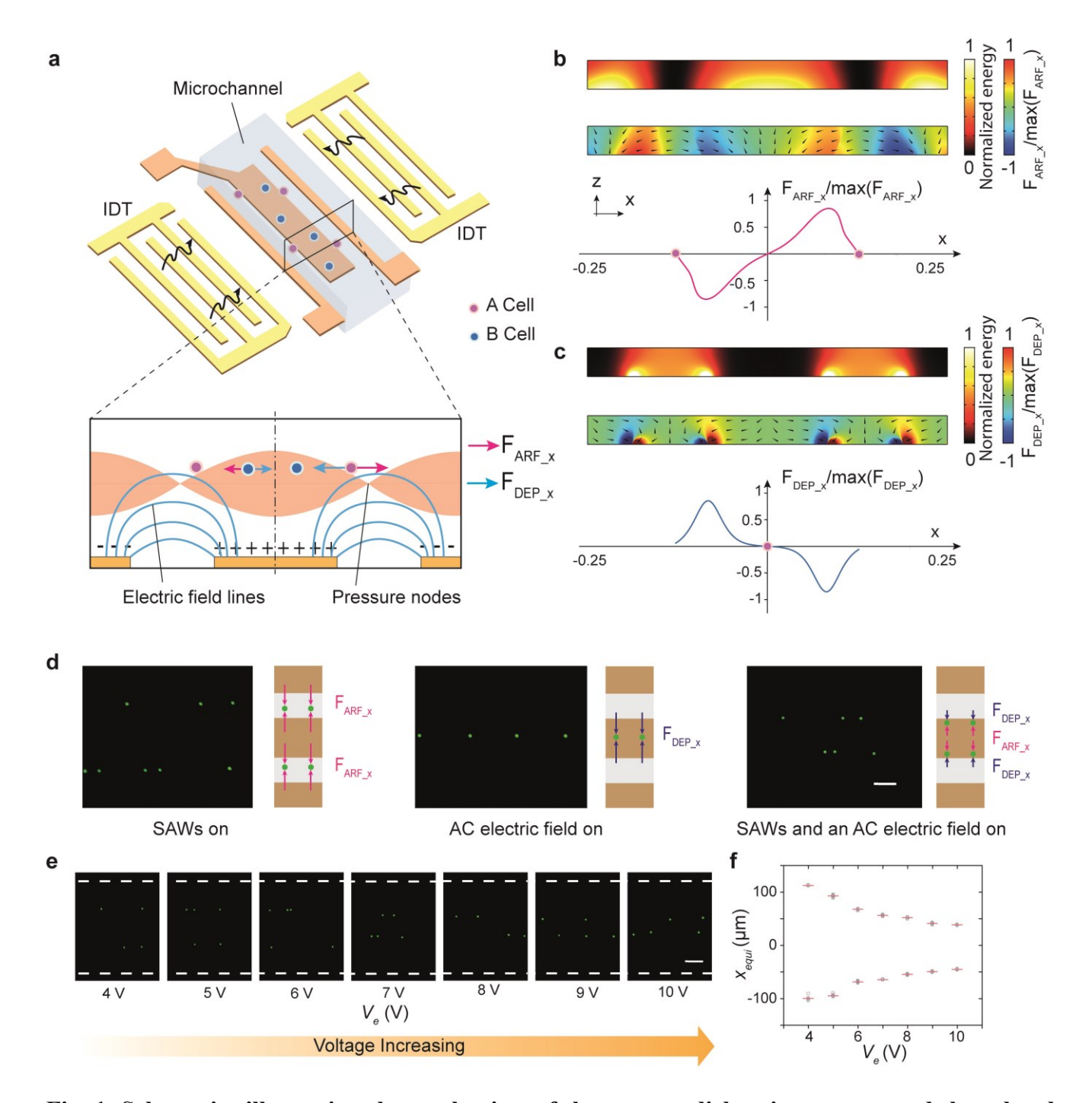


Fig. 1. Schematics illustrating the mechanism of the acousto-dielectric tweezers and the related numerical and experimental results. (a) A schematic of an acousto-dielectric chip composed of a pair of IDTs on a LiNbO₃ wafer used to generate standing SAWs and parallel tri-port electrodes used to generate AC electric fields in a microchannel. As illustrated in the cross-section schematic, two cell

types (A and B) experience both the acoustic radiation forces F_{ARF-x} applied by standing SAWs as well as the DEP forces F_{DEP-x} induced by an AC electric field. Under these forces, two cell types with different biophysical properties can be trapped at different equi-acousto-dielectric positions x_{equi} , where F_{ARF-x} $(x_{equi}) = -F_{DEP-x}(x_{equi})$. (b) Simulation results showing the tweezing mechanism with only standing SAWs present. The top, middle, and bottom subplots are the simulated fluid-domain acoustic energy field, the corresponding x-component acoustic radiation force F_{AFR-x} field for manipulating polystyrene microparticles, and the x-component force distribution along the microchannel top (i.e., $z = 40 \mu m$), respectively. (c) Simulation results showing the tweezing mechanism with only an AC electric field present. The top, middle, and bottom subplots are the simulated fluid-domain electric energy field, the corresponding x-component DEP force F_{DEP-x} field for manipulating polystyrene microparticles, and the x-component force distribution along the microchannel top (i.e., $z = 40 \mu m$), respectively. The colors and arrows in the middle subplots of **b** and **c** indicate x-component force values and directions of the force vectors, respectively. (d, left) A captured microscopy image showing polystyrene microparticles trapped by two pressure node lines when only standing SAWs were generated by the IDTs. (d, middle) A captured microscopy image showing polystyrene microparticles trapped at the microchannel center when only an AC electric field was generated by the tri-port electrodes. (d, right) A captured microscopy image showing polystyrene microparticles trapped at equi-acousto-dielectric positions x_{equi} , when both standing SAWs and an AC electric field were generated. (e) Captured microscopy images showing polystyrene microparticles gradually translating towards the center of the microchannel by increasing the input voltage V_e for tri-port electrodes. (f) Equi-acousto-dielectric positions measured from acquired microscopy images at various DEP voltages V_e (circles: measured position, red bar: average position, n = 11). Scale bars in **d** and **e**: 100 μ m.

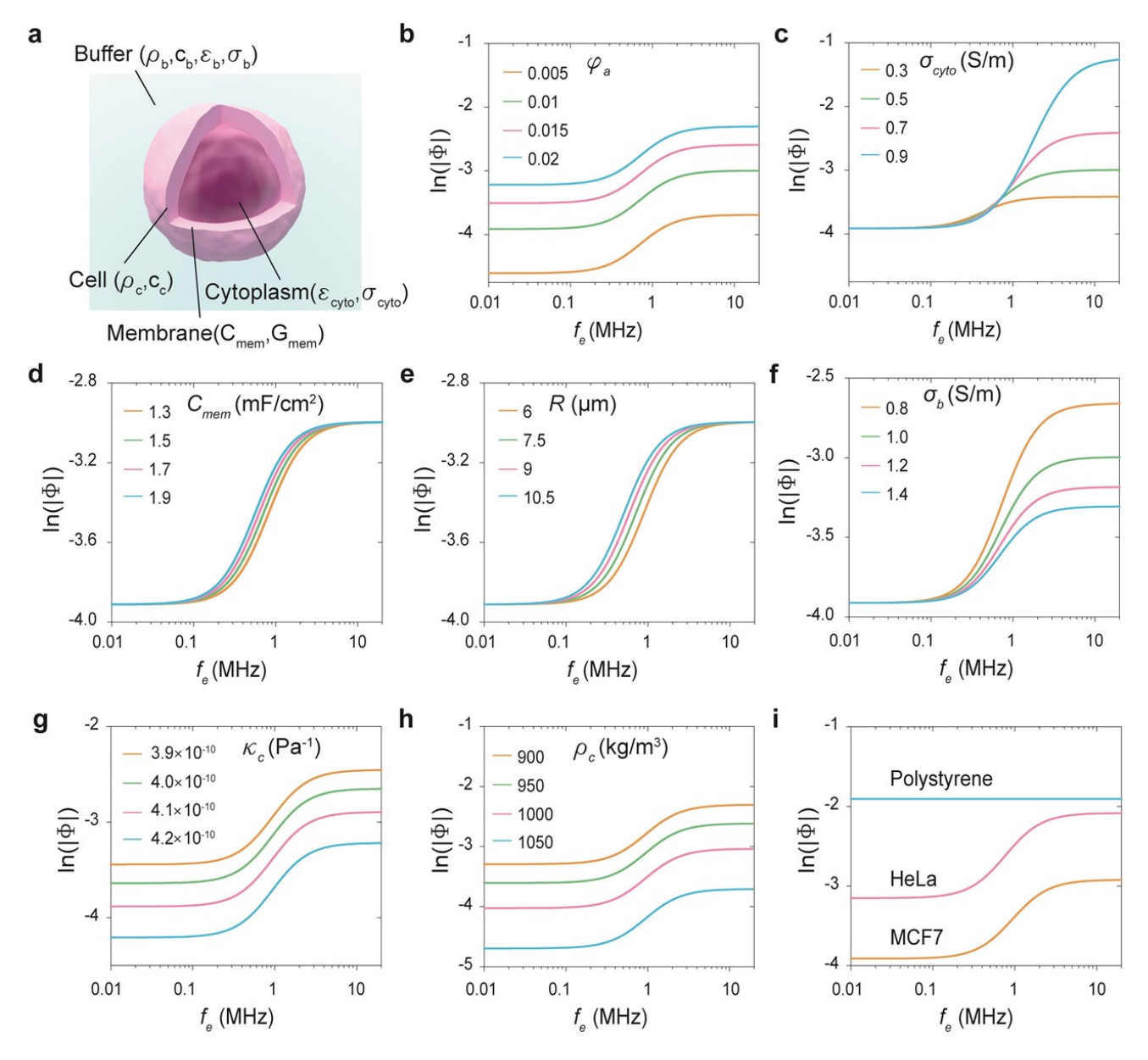


Fig. 2. Theoretical acousto-dielectric factors for different cell and buffer properties. (a) Schematics of effective acousto-mechanical and electrical models of a cell in a buffer. (b-f) Individual effects of the acoustic contrast factor φ_a , cytoplasm conductivity σ_{cyto} , membrane capacitance C_{mem} , cell radius R, and buffer conductivity σ_b on acousto-dielectric factors at different DEP frequencies. To obtain each plot, only one of the aforementioned parameters is changed, while the remaining parameters are selected from predetermined constants (e.g, $\varphi_a = 0.01$, $\sigma_{cyto} = 0.5$ S/m, $C_{mem} = 1.5$ mF/cm², R = 7.5 μm, and $\sigma_b = 1$ S/m). (g, h) Effects of the cell compressibility κ_c and density ρ_c on the acousto-dielectric factors. (i) Acousto-dielectric factors for polystyrene particles, HeLa cells, and MCF7 cells with the same radius of 8 μm. The properties used for calculating acousto-dielectric factors are listed in Supplementary Table 1.

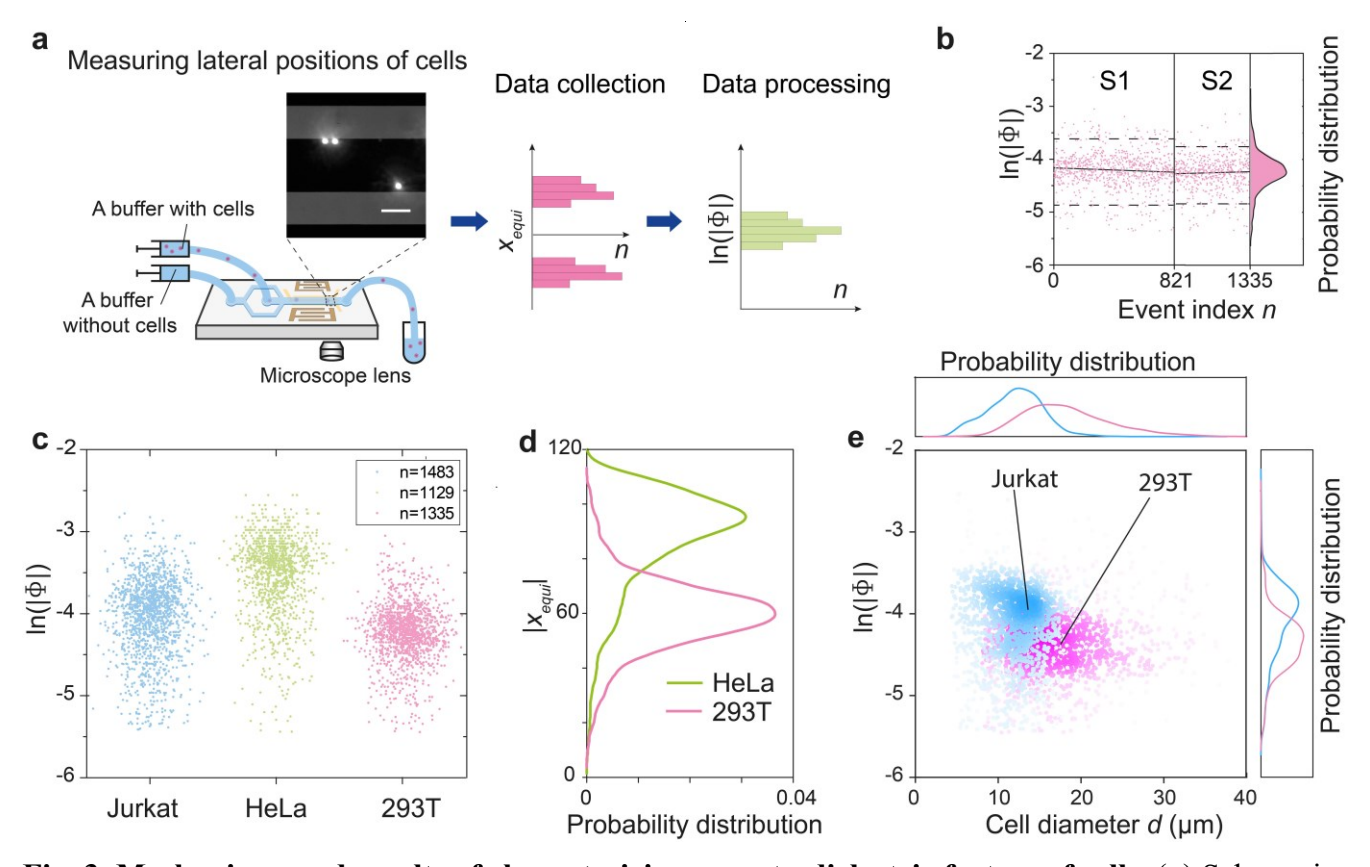


Fig. 3. Mechanisms and results of characterizing acousto-dielectric factors of cells. (a) Schematics showing the experimental setup and procedures necessary to characterize acousto-dielectric factors. When cells in a buffer flowed through the microchannel of our chip, the acoustic radiation and DEP forces gradually pushed the cells to their corresponding equi-acousto-dielectric positions. These positions (denoted as $[x_{equi,n}]_N$) can be measured using microscopy images of a region near the channel outlet. By referring to the calibrated acousto-dielectric field function $\Psi_c(x)$, the acousto-dielectric factors $[\Phi_n]_N$ of cells can be determined with $\Phi_n = \Psi_c(x_{equi,n})$. Calcein-AM was used for showing live cells. Scale bar: 100 μ m. (b) The measured acousto-dielectric factors for 293T cells from two experiments (with n =821 and 514, respectively) and their overall probability density distribution (p-value = 0.001). The dashed lines show the 5th and 95th percentiles. The solid lines represent the linear least-square fitting results (group S1: slope = -1.09×10^{-4} , correlation coefficient = -0.073; group S2: slope = -7.508×10^{-5} , correlation coefficient = -0.034). (c) Scatter plots showing measured equi-acousto-dielectric factors for Jurkat (n = 1483), HeLa (n = 1129), and 293T cells (combination of two experiments with n = 821 and 514, respectively). (d) Probability density distributions of HeLa and 293T cells with respect to their equilibrium positions. The two cell populations, which have similar diameters, are spatially distributed in different groups. This observation indicates that our approach has the potential to achieve sizeinsensitive cell separation. (e) Scatter plots showing measured acousto-dielectric factors versus the

diameters of Jurkat and 293T cells. The scatter plots for these two cell populations are distributed in different clusters, indicating that our approach can potentially be used for cell phenotyping.

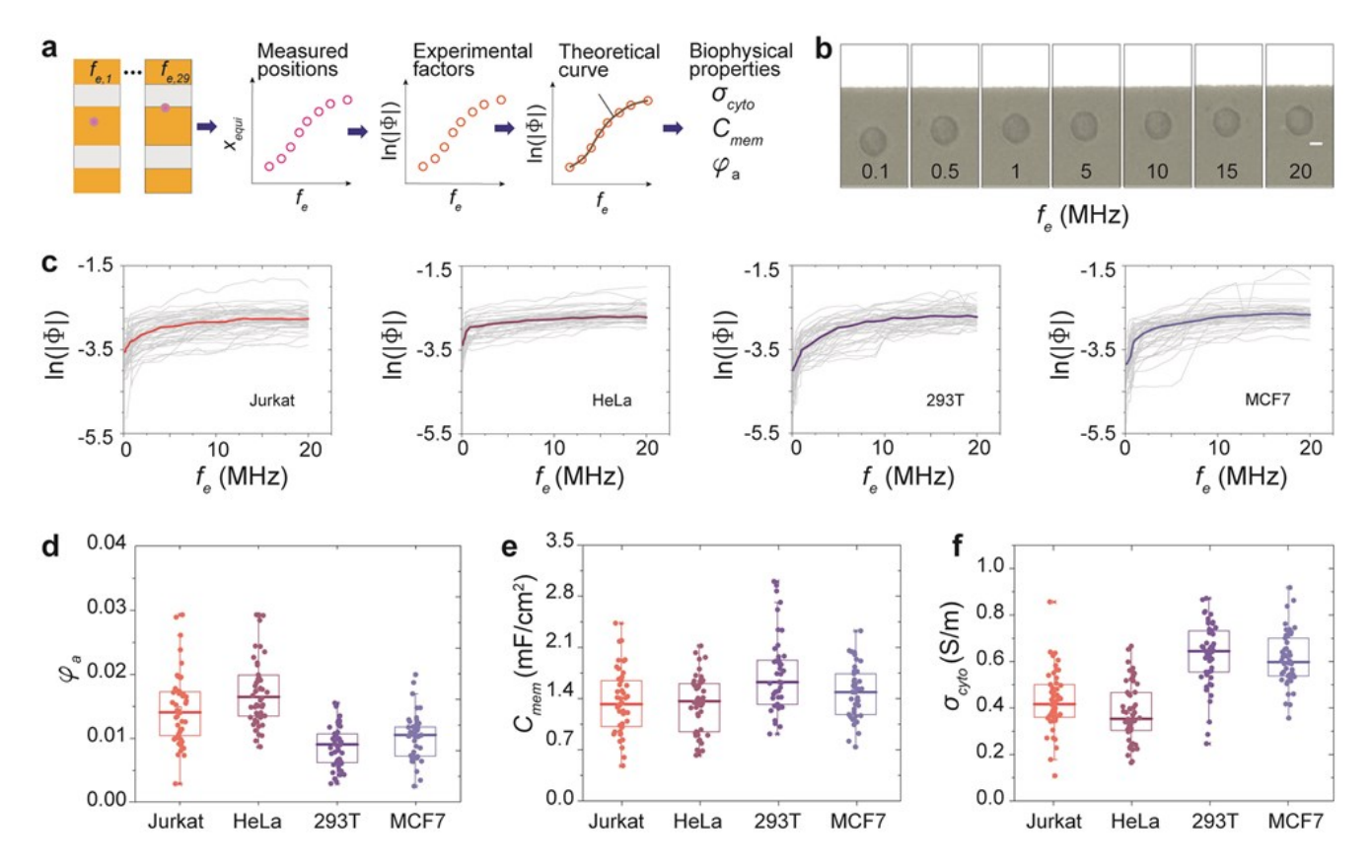


Fig. 4. Mechanism and results of quantitatively characterizing the acousto-mechanical and electrical properties of cells. (a) Schematics illustrating the procedures used to characterize the acoustic contrast factor φ_a , cytoplasm conductivity σ_{cyto} , and membrane capacitance C_{mem} of a cell. Initially, at conditions with different AC electric field frequencies $[f_{e,m}]_M$ (M total number of frequencies, m frequency index), the equi-acousto-dielectric positions $[x_{equi,m}]_M$ and acousto-dielectric factors $[\Phi_m]_M$ were measured. Next, a theoretical $\ln|\Phi| - f_e$ relation that best fits experimentally acquired $[\ln|\Phi|_m]_M - [f_{e,m}]_M$ data was determined through regression. The properties φ_a , σ_{cyto} , and C_{mem} measured by our approach, which correspond to the theoretical relation, were saved as the cell's properties. (b) Microscopy images showing cells at different equi-acousto-dielectric positions at conditions with different AC electric field frequencies. Scale bars: $10 \ \mu m$. (c) Measured acousto-dielectric factors versus AC electric field frequencies for four cell types (left to right: Jurkat, HeLa, 293T, and MCF7 cells). (d-

f) Scatter plots of the measured acoustic contrast factor, membrane capacitance, and cytoplasm conductivity, respectively (n = 50).